

Research Paper

Superellipsoid-based study on reproducing 3D particle geometry from 2D projections

Xiang Wang^{a,c}, Kanglin Tian^a, Dong Su^{b,*}, Jidong Zhao^c^a Department of Civil Engineering, Central South University, Changsha, Hunan, China^b College of Civil and Transportation Engineering, Shenzhen University, Shenzhen, China^c Department of Civil and Environmental Engineering, Hong Kong University of Science and Technology, Hong Kong, China

ARTICLE INFO

Keywords:

Granular media
 Geometry prediction
 Particle size
 Particle shape
 Superellipsoids
 Particle scanning

ABSTRACT

The potential of reproducing the 3D geometrical features, e.g., sizes, elongation and flatness, of idealized convex granular particles from their 2D random projections was investigated based on a superellipsoid model. Using the random projection method, the relationships between the geometrical features of monosized superellipsoids and the statistical distributions of the corresponding 2D projected counterparts were examined. The 2D size parameters, e.g., r_{1max} , r_{mean} and r_{2min} , obtained from the projected images were well correlated with the semi-axial principal dimensions of the 3D particles, e.g., R_1 , R_2 and R_3 . Further studies of randomised superellipsoid particles with various aspherical shapes and limited projection numbers were performed to validate the findings. The capability and reliability of predicting 3D sizes and shapes from 2D projections were statistically analysed and verified. The correlation of prediction accuracy with increasing projection number and varied aspherical shapes was investigated. Based on the results, a particle geometry prediction framework was proposed, and the associated performance was examined using realistic cobble particles obtained from 3D laser scanning. The promising results highlight the potential of this approach in future industrial applications.

1. Introduction

A particle can be defined as an individual three-dimensional body in a dispersed system of granular assemblies. In addition to the chemical and mineral constitution of a particle, geometric features, including particle size [1–3] and shape [4–6], significantly affect the macroscopic behaviours of granular materials, e.g., packing properties [7–9], shear strength [10–12], stiffness [13,14] and other factors. To better understand the relationships between particle geometries and the corresponding granular behaviours, particle geometry quantification [15–19] and reconstruction [20–22] are two prerequisite procedures that have become the focus of a considerable body of research. In the laboratory, numerous methods, such as laser particle size analyser (LPSA), segmentation-based gradation analyser (SGA), electrical resistance particle counter (ERPC), particle digital image processor (PDIP) methods, are used to characterise particle geometries. LPSAs, SGAs and ERPCs are capable of measuring particle size parameters but are unable to estimate the shapes of particles. Although PDIPs can provide information on both types of descriptors, there are several drawbacks to traditional PDIP methods. (1) The dispersion degree of

particles is often insufficient, which leads to contact and overlap among grains and influences the accuracy of particle analysis. (2) Particles remain static, and the orientations of aspherical grains result in statistical divergence. Thanks to advanced measurement technologies, dynamic imaging apparatuses (such as the Sympatec QICPIC analyser [23]) have been developed to overcome these drawbacks and satisfy research demands. These technologies enable researchers to sample one particle from different viewpoints, which considerably increases the number of 2D projections. Thus, compared to static analysis, dynamic imaging eliminates the orientation error and guarantees high representativeness and reproducibility.

With the aid of dynamic imaging systems, statistical results of 2D sizes and shapes can be easily and quickly obtained for both research and industrial uses. Many researchers [19,24–31] have employed the size and shape results from dynamic imaging systems (e.g., the QICPIC analyser) to quantify the relationships among the properties of granular particles. Cavarretta et al. [31] evaluated the circularity and aspect ratio of cohesion-less granular materials using QICPIC. Sandler and Wilson [30] employed QICPIC to acquire the Feret diameter, sphericity, convexity and aspect ratio of particulate pharmaceutical materials. The

* Corresponding author at: College of Civil and Transportation Engineering, Shenzhen University, Shenzhen, China. Underground Polis Academy, Shenzhen University, Shenzhen, China.

E-mail addresses: wang.xiang@csu.edu.cn (X. Wang), tiankanglin@csu.edu.cn (K. Tian), sudong@szu.edu.cn (D. Su), jzhao@ust.hk (J. Zhao).

<https://doi.org/10.1016/j.compgeo.2019.103131>

Received 29 January 2019; Received in revised form 25 April 2019; Accepted 10 June 2019

0266-352X/© 2019 Elsevier Ltd. All rights reserved.

particle shape parameters obtained with the QICPIC analyser were used by Altuhafi and Coop [28] to explore the micromorphological changes in sands under compression and shearing. Among these experimental studies, it is often hypothesised that, with numerous 2D images of the same particle, the sizes and shapes of 3D particles can be inferred with high confidence. However, very few studies have been performed to examine this hypothesis. Kuo et al. [32] illustrated that the 3D dimensions and shapes of particles can be measured using three orthogonal projections. Based on this concept, Ken et al. [33] developed a triaxial viewer and found that the correlations between 3D and 2D results are influenced by the orientation of the randomly positioned particle. The uncertainty of this approach was minimised by rotating particles with optimised orientations based on an analysis of the principal moment of inertia and the vertical image of a particle with an image analysis system. However, the orthogonal projection method is applicable only when dealing with large particles and small particle quantities. Kutay et al. [34] investigated the relationships between 2D and 3D shape indices among five categories of aggregates (natural gravel, basalt, granite, diabase and slate). The 2D images were obtained using AIMS, and the 3D particle models were acquired from X-ray CT. The correlation results illustrated significant scatter because the AIM system is a static imaging system and cannot obtain enough projection images to conduct representative statistical analyses of 2D shapes. Regarding the prediction of 3D geometries from dynamically imaged 2D projections, Fonseca et al. [35] compared the 2D distributions of particle sizes and shapes with the 3D results obtained from micro-CT data. The results indicated that the maximum Feret diameters of the 2D projections closely approximate the major dimensions of the 3D particles, while the 2D distributions of aspect ratio (AR) do not correlate well with any of the 3D measures. Additionally, Yan and Su [36] employed the ellipsoid particle model to reveal the potential correlation between the 2D average radius and 3D average radius of the original particles. Then, they presented a novel method for predicting the values of the elongation index (EI) and flatness index (FI) of 3D particles based on the statistical distribution of the AR values of the projected 2D images [37]. For realistic particles, however, ellipsoids sometimes fail to describe the particle shape due to the lack of details that reflect angularity. Ueda et al. introduced roughness features into ellipsoid models and employed a genetic algorithm (GA) to establish a conversion database between 3D and 2D parameter distributions [38]. However, their GA-based model was specific to the adopted learning samples. Moreover, the randomly generated ellipsoids with superimposed Gaussian noise-based roughness exhibited an unrealistic appearance compared with the real particle shape irregularities. When applying this method to a particular type of granular particles, to achieve high prediction accuracy, a large learning sample, e.g., 100,000 real particles, might be required to train the GA model. Thus, the applicability of using 2D shape results to infer detailed 3D geometries (e.g., the longest, intermediate and shortest semi-axis lengths; elongation; flatness) remains a research question. Nevertheless, to date, there is no solution for large geomaterials, e.g., aggregates and ballasts, since the existing dynamic imaging system (QICPIC) is limited to sand-sized particles. An alternative method could involve using a high-speed camera to acquire random projections of aggregate when particles fall and roll. However,

some questions must be addressed when considering this alternative: (1) How can the obtained 2D projections of each particle be used to interpret the 3D size and shape of the particle? (2) How will shape asphericity and limited projection numbers influence the relationship between 2D geometries and the corresponding 3D geometries?

In this study, based on the numerical ellipsoid approach proposed by Yan and Su [36,37], a superellipsoid model is employed to investigate the capability and accuracy of reproducing the 3D sizes and shapes of particles with descriptors derived from 2D images. First, three typical geometries (prolate, oblate and scalene) of monosized superellipsoids are generated with three different aspherical shapes (cubic, spheroid and octahedral) and then randomly projected into numerous 2D images. From the projected images, statistical analyses of the 2D sizes and shapes are conducted to study their correlations with the corresponding 3D sizes and shapes. Second, several hypotheses are proposed to infer the three semi-axial principal dimensions (R_1 , R_2 , and R_3) and shapes (EI and FI) with 2D projections. The proposed hypotheses are then verified through analyses of randomised superellipsoids and the realistic particles obtained from 3D laser scanning to investigate the influences of aspherical shape variations and limited projection numbers on the applicability of the proposed hypotheses.

2. Generation, projection and geometry quantification of superellipsoids

2.1. Mathematical expression of superellipsoids

A superellipsoid is the three-dimensional version of a superellipse, which is in turn a cross between a square and a circle. Superellipsoids have been employed by researchers to capture many of the essential features of real particle shapes [39]. The surface function of a superellipsoid centred at the origin of a Cartesian coordinate system can be defined as follows [40]:

$$\left| \frac{x}{a} \right|^{\frac{2}{1-\varepsilon}} + \left| \frac{y}{b} \right|^{\frac{2}{1-\varepsilon}} + \left| \frac{z}{c} \right|^{\frac{2}{1-\varepsilon}} = 1 \quad (1)$$

where ε is referred to as the index of shape asphericity and a , b and c denote the semi-principal lengths along the x -, y - and z -axes, respectively. To generate the 3D numerical model of a superellipsoid, a polar representation is used in this study. Given the local spherical coordinate (θ, φ) of a point on the particle surface, the corresponding local Cartesian coordinate (x, y, z) can be expressed as follows:

$$\begin{cases} x(\theta, \varphi) = \text{Sign}(\cos(\theta))a |\cos(\theta)|^{1-\varepsilon} |\cos(\varphi)|^{1-\varepsilon} \\ y(\theta, \varphi) = \text{Sign}(\sin(\theta))b |\sin(\theta)|^{1-\varepsilon} |\cos(\varphi)|^{1-\varepsilon} \\ z(\theta, \varphi) = \text{Sign}(\sin(\varphi))c |\sin(\varphi)|^{1-\varepsilon} \end{cases} \quad (2)$$

where term $\text{Sign}(x)$ is the signum function, which can be defined as follows.

$$\text{Sign}(x) = \begin{cases} -1 & \text{if } x < 0, \\ 0 & \text{if } x = 0, \\ 1 & \text{if } x > 0. \end{cases} \quad (3)$$

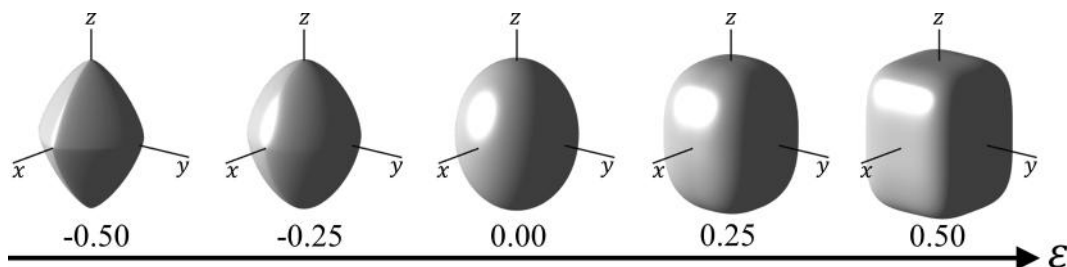


Fig. 1. 3D views of superellipsoid shapes varying with ε when $a = b = 1$ and $c = 1.25$

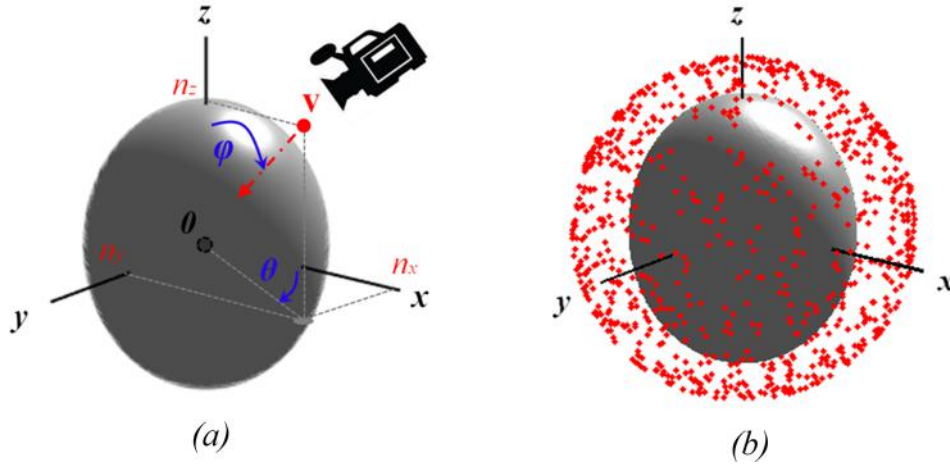


Fig. 2. (a) unit vector \mathbf{v} in the Cartesian coordinate system; (b) 1000 random vectors for particle projection.

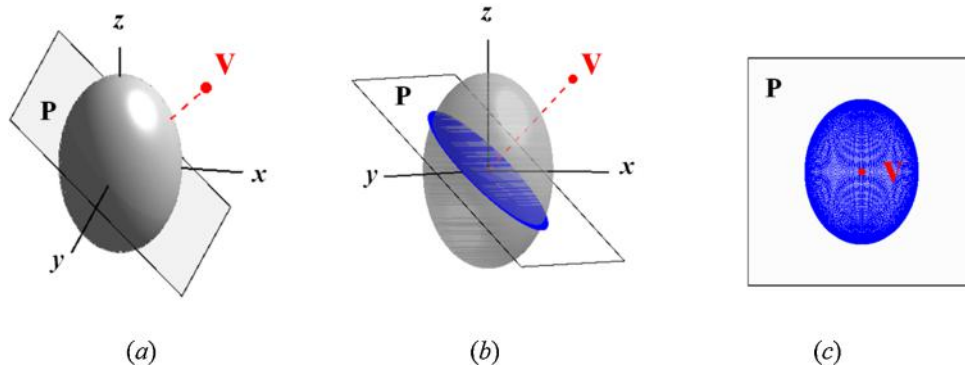


Fig. 3. (a) projection plane P of vector \mathbf{v} ; (b) projection of surface points in the direction of vector \mathbf{v} onto plane P; (c) plan view of the projected surface points on plane P.

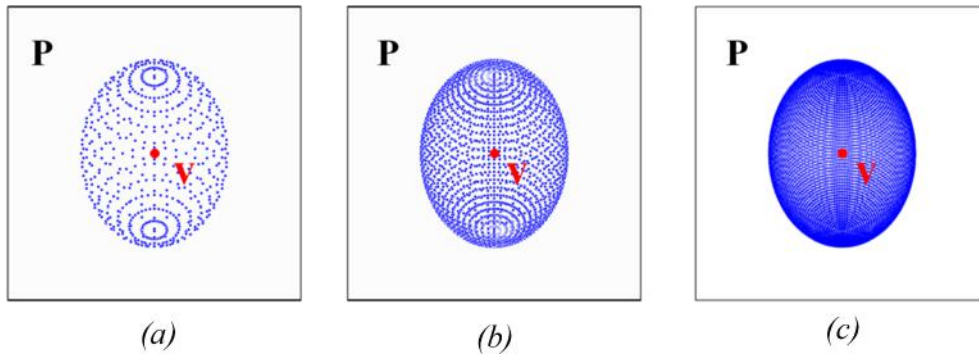


Fig. 4. Plan view of projective surface points on plane P with (a) $n = 703$; (b) $n = 2701$; and (c) $n = 16471$

As illustrated in Fig. 1, changing ϵ yields a wide range of shapes: $\epsilon \rightarrow 0.5$ produces a cubic shape, and $\epsilon \rightarrow -0.5$ corresponds to an octahedral shape. In particular, $\epsilon = 0$ yields a perfect spheroid shape. The proposed superellipsoid model provides a broad range of aspherical irregular particle shapes, smoothly transitioning through a range of surface curvatures (by changing ϵ) and aspect ratios (by changing a , b and c). Through this approach, we can explore how the degree of irregular shape variations affects the prediction accuracy of 3D particle geometries with 2D images.

2.2. Computation of random projected images

As stated by Yan and Su [36,37], particle scanning in most dynamic imaging systems can be regarded as projecting particles in random

directions to obtain projected images due to the extremely short scanning time and insignificant air buoyancy effect when randomly orientated particles are dropped into the scanner.

As shown in Fig. 2a, the vector $\mathbf{v}(n_x, n_y, n_z)$ representing the projection direction in the Cartesian coordinate system can be obtained from the spherical coordinate vector $\mathbf{v}'(\theta, \varphi, r)$. This conversion can be expressed as follows.

$$\begin{cases} n_x = \cos(\theta) \sin(\varphi)r \\ n_y = \sin(\theta) \cos(\varphi)r \\ n_z = \cos(\varphi)r \end{cases} \quad (4)$$

In this case, θ and φ for a random unit vector in 3D space can be generated as follows [36,37]:

Table 1
Geometry data of the generated monosized superellipsoids.

Geometry type	Asphericity type	Longest, Intermediate and Shortest semi-axis lengths			Particle name
		R ₁	R ₂	R ₃	
Prolate R ₁ > R ₂ = R ₃	Cubic ε = 0.5	1.5	1	1	C[1.5/1/1]
		2.0	1	1	C[2.0/1/1]
		2.5	1	1	C[2.5/1/1]
		3.0	1	1	C[3.0/1/1]
	Spheroid ε = 0.0	1.5	1	1	S[1.5/1/1]
		2.0	1	1	S[2.0/1/1]
		2.5	1	1	S[2.5/1/1]
		3.0	1	1	S[3.0/1/1]
	Octahedral ε = -0.5	1.5	1	1	O[1.5/1/1]
		2.0	1	1	O[2.0/1/1]
		2.5	1	1	O[2.5/1/1]
		3.0	1	1	O[3.0/1/1]
Oblate R ₁ > R ₂ = R ₃	Cubic ε = 0.5	1.5	1.5	1	C[1.5/1.5/1]
		2.0	2.0	1	C[2.0/2.0/1]
		2.5	2.5	1	C[2.5/2.5/1]
		3.0	3.0	1	C[3.0/3.0/1]
	Spheroid ε = 0.0	1.5	1.5	1	S[1.5/1.5/1]
		2.0	2.0	1	S[2.0/2.0/1]
		2.5	2.5	1	S[2.5/2.5/1]
		3.0	3.0	1	S[3.0/3.0/1]
	Octahedral ε = -0.5	1.5	1.5	1	O[1.5/1.5/1]
		2.0	2.0	1	O[2.0/2.0/1]
		2.5	2.5	1	O[2.5/2.5/1]
		3.0	3.0	1	O[3.0/3.0/1]
Scalene R ₁ > R ₂ > R ₃	Cubic ε = 0.5	1.44	1.2	1	C[1.44/1.2/1]
		1.96	1.4	1	C[1.96/1.4/1]
		2.56	1.6	1	C[2.56/1.6/1]
		3.24	1.8	1	C[3.24/1.8/1]
	Spheroid ε = 0.0	1.44	1.2	1	S[1.44/1.2/1]
		1.96	1.4	1	S[1.96/1.4/1]
		2.56	1.6	1	S[2.56/1.6/1]
		3.24	1.8	1	S[3.24/1.8/1]
	Octahedral ε = -0.5	1.44	1.2	1	O[1.44/1.2/1]
		1.96	1.4	1	O[1.96/1.4/1]
		2.56	1.6	1	O[2.56/1.6/1]
		3.24	1.8	1	O[3.24/1.8/1]

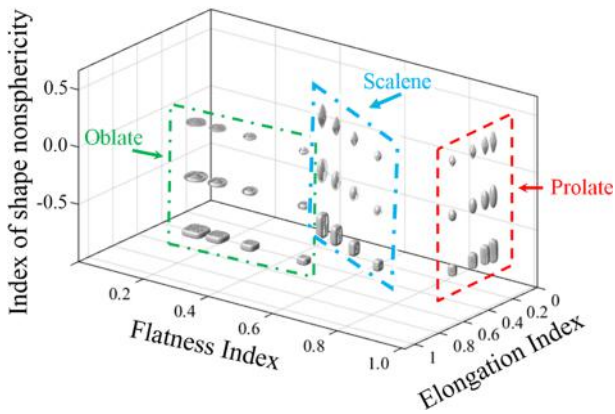


Fig. 5. Visualisation of the generated 3D superellipsoids in a Zingg diagram.

$$\begin{cases} \theta = 2\pi\xi_1 \\ \varphi = \arccos(1 - 2\xi_2) \end{cases} \quad (5)$$

where ξ_1 and ξ_2 are two uniformly distributed random variables in the range [0,1]. As shown in Fig. 2b, 500 random vectors are generated for particle projections. The generated projection vectors have random orientations and are uniformly distributed around the target object in 3D space.

Given a specific projection vector $\mathbf{v}(n_{x0}, n_{y0}, n_{z0})$, the corresponding projection plane P (shown in Fig. 3a) passing through the origin can be expressed as follows.

$$n_{x0}x + n_{y0}y + n_{z0}z = 0 \quad (6)$$

It is assumed that a surface point $Q(x_0, y_0, z_0)$ is projected onto plane P of vector $\mathbf{v}(n_{x0}, n_{y0}, n_{z0})$. The corresponding projective point $Q'(x'_0, y'_0, z'_0)$ can be obtained by solving the following equation.

$$\begin{cases} n_{x0}x'_0 + n_{y0}y'_0 + n_{z0}z'_0 = 0 \\ \frac{x_0 - x'_0}{n_{x0}} = \frac{y_0 - y'_0}{n_{y0}} = \frac{z_0 - z'_0}{n_{z0}} \end{cases} \quad (7)$$

As shown in Fig. 3b, n surface points $\{Q_1, \dots, Q_i, \dots, Q_n\}$ are uniformly sampled from the superellipsoid ($a = b = 1, c = 1.5, \varepsilon = 1$) and then projected in the direction of the projection vector $\mathbf{v}(1, 1, 1)$ onto the plane P. The plane view of the obtained projected points $\{Q'_1, \dots, Q'_i, \dots, Q'_n\}$ on plane P is shown in Fig. 3c. Fig. 4 shows that the cluster of obtained projected points approximates the 2D projection image as the number (n) of sampled surface points increases. In this study, $n = 16471$ is adopted for particle generation to ensure that the 2D geometries measured from the obtained projected points are identical to those of the real 2D projection image.

2.3. Quantification of particle sizes and shapes

For a superellipsoid, the 3D particle size can be characterised by three descriptors, namely, R_1, R_2 and R_3 , which denote the longest, intermediate and shortest semi-axis lengths.

$$\begin{cases} R_1 = \max(a, b, c) \\ R_2 = \text{mid}(a, b, c) \\ R_3 = \min(a, b, c) \end{cases} \quad (8)$$

After acquiring R_1, R_2 and R_3 , the 3D particle shapes of a superellipsoid can be described using two descriptors, EI and FI, [41] which represent the elongation index and flatness index, respectively.

$$\begin{cases} EI = R_2/R_1 \\ FI = R_3/R_2 \end{cases} \quad (9)$$

For each projected image of a superellipsoid, we can measure two size parameters, e.g., r_1 and r_2 , which can be obtained by measuring the semi-length of the major and minor axes of the circumscribed rectangle using the bounding box method [22]. Subsequently, the aspect ratio (AR) of a 2D particle projection is computed as follows.

$$AR = \frac{r_2}{r_1} \quad (10)$$

Based on these definitions, AR (which also applies to EI and FI) varies from 0 and 1, and a more equant shape is obtained as AR increases.

Additionally, if n number of projections of one superellipsoid are acquired, three sets of 2D size and shape parameters can be obtained, including $\{r_{11}, \dots, r_{1i}, \dots, r_{1n}\}, \{r_{21}, \dots, r_{2i}, \dots, r_{2n}\}$ and $\{AR_1, \dots, AR_i, \dots, AR_n\}$. Based on this 2D data, the following 2D indices can be computed:

$$r_{1max} = \max(r_{11}, \dots, r_{1i}, \dots, r_{1n}) \quad (11)$$

$$r_{1min} = \min(r_{11}, \dots, r_{1i}, \dots, r_{1n}) \quad (12)$$

$$r_{2max} = \max(r_{21}, \dots, r_{2i}, \dots, r_{2n}) \quad (13)$$

$$r_{2min} = \min(r_{21}, \dots, r_{2i}, \dots, r_{2n}) \quad (14)$$

$$AR_{max} = \max(AR_1, \dots, AR_i, \dots, AR_n) \quad (15)$$

$$AR_{min} = \min(AR_1, \dots, AR_i, \dots, AR_n) \quad (16)$$

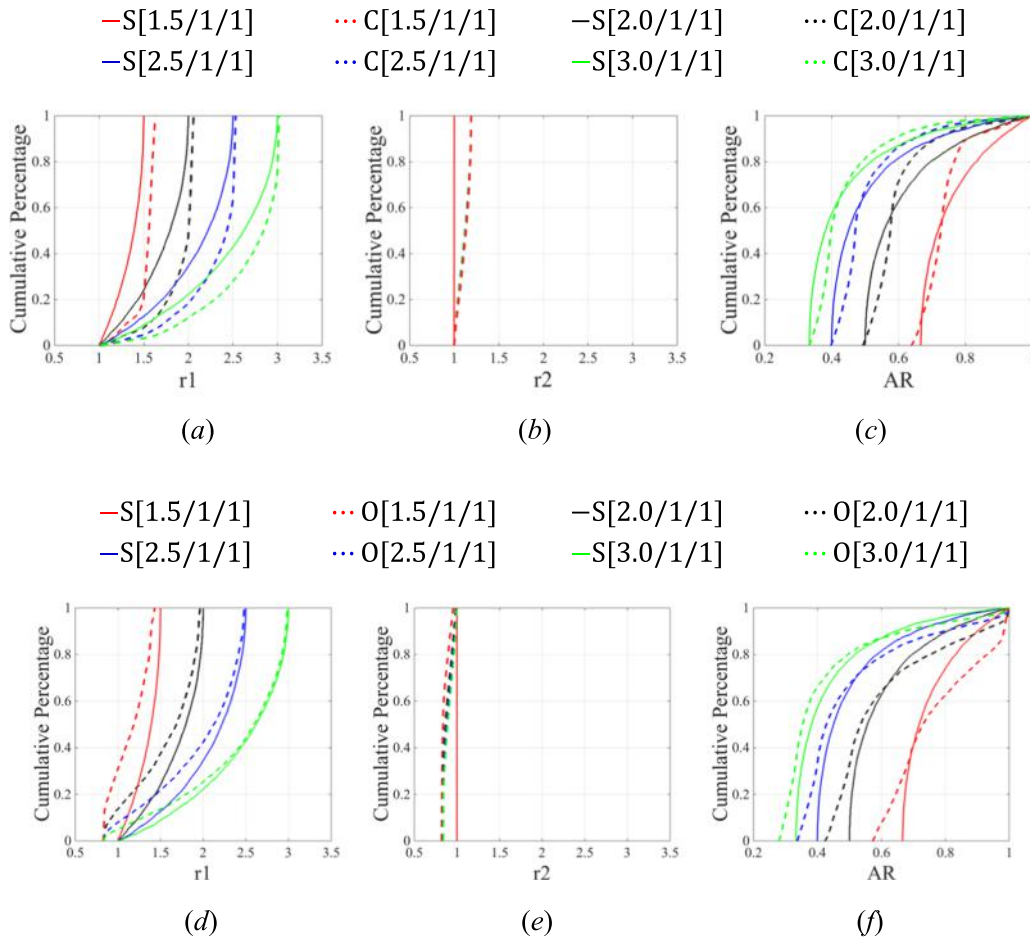


Fig. 6. Comparison of prolate superellipsoids involving spheroids (denoted as S with solid lines) with cubic (denoted as C with dotted lines) (a)–(c) and octahedral (denoted as O with dotted lines) (d)–(f) shapes.

3. Study of monosized superellipsoids with specific geometries

In nature, particles can have various sizes and shapes. To simplify the problem, monosized superellipsoids (with the same minimum principal dimension) with three typical shapes, e.g., cubic ($\varepsilon = 0.5$), spheroidal ($\varepsilon = 0$), and octahedral ($\varepsilon = -0.5$), and three specific geometries, e.g., prolate ($R_1 > R_2 = R_3$), oblate ($R_1 = R_2 > R_3$), and scalene ($R_1 > R_2 > R_3$), are generated. The sizes and shapes of the generated superellipsoids are listed in Table 1. As shown in Fig. 5, the generated 3D superellipsoids are plotted in a Zingg diagram for visualisation and comparison. To better understand the relationships between the 3D geometries and the 2D projected results, each particle with a given geometry is randomly projected into 5000 images for statistical analysis. The same number of projections was also employed to study the statistics of ellipsoids by previous researchers [36,37]. This process mimics the experiment in which a single particle is analysed with a scanner to obtain a large quantity of 2D random projections. Then, the 2D sizes and shapes of all projected particles are measured for statistical analysis.

3.1. Statistical results of 2D projections

3.1.1. Case I: Monosized prolate superellipsoids

Fig. 6a–c compares the cumulative distribution curves of the 2D sizes (r_1 , r_2) and aspect ratio (AR) of monosized prolate superellipsoids for $\varepsilon = 0.5$ (cubic shape) and $\varepsilon = 0$ (spheroid shape). Generally, both r_1 and AR exhibit broader distributions when the $EI = \frac{R_2}{R_1}$ value of the prolate superellipsoid decreases. For both cubic and spheroid shapes

(shown in Fig. 6a), the cumulative distribution curves of r_1 present relatively moderate gradients at $r_1 \approx r_{1min}$ and very steep gradients at $r_1 \approx r_{1max}$. This phenomenon reflects the high proportion of r_1 values clustered around their largest value r_{1max} . Additionally, when EI decreases (R_1 increases), the r_{1max} values of cubic shapes approach R_1 . As demonstrated in Fig. 6b, the spheroid-shaped particles present $r_{2max} = r_{2min} = R_2 = R_3 = 1$, and the r_2 curves of cubic-shaped particles overlap and illustrate a steep slope within $r_2 \in [1.0, 1.2]$. In contrast to r_1 , the AR curves of both spheroid and cubic shapes display steep gradients at $AR \approx AR_{min}$. The gradients become moderate as AR approaches $AR_{max} = FI = \frac{R_3}{R_2} = 1$.

As shown in Fig. 6d–f, the monosized prolate superellipsoids with $\varepsilon = -0.5$ (octahedral shape) and $\varepsilon = 0$ (spheroid shape) are statistically compared. As shown in Fig. 6d, the maximum value of r_1 for the octahedral superellipsoids becomes increasingly similar to that of the spheroid superellipsoids as R_1 increases (EI decreases). For r_2 , the octahedral superellipsoid exhibits a steep slope with the values varying from 0.8 to 1.0. Similar to the cubic case, the distribution of AR in the octahedral superellipsoid case is similar to that in the spheroid case when EI decreases (R_1 increases). In all cases, AR_{max} is always equal to $FI = \frac{R_3}{R_2} = 1$.

3.1.2. Case II: Monosized oblate superellipsoids

Fig. 7 shows the cumulative distribution curves of the 2D sizes (r_1 , r_2) and ARs of monosized oblate superellipsoids for $\varepsilon = -0.5, 0$, and 0.5. Generally, similar to prolate superellipsoids, r_2 and AR exhibit broad variations as the $FI = \frac{R_3}{R_2}$ value of the 3D superellipsoid decreases. As shown in Fig. 7a, r_1 of spheroid superellipsoids always equals R_1 , and for

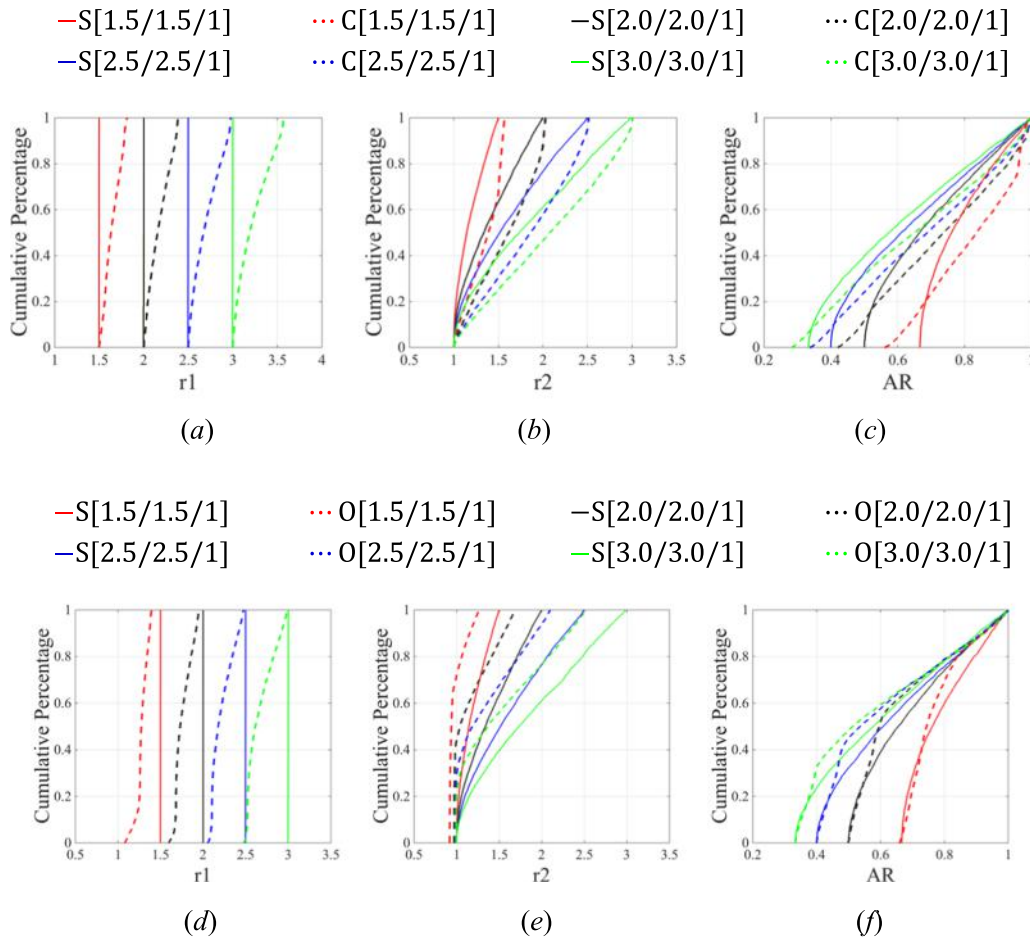


Fig. 7. Comparison of oblate superellipsoids involving spheroids (denoted as S with solid lines) with cubic (denoted as C with dotted lines) (a)–(c) and octahedral (denoted as O with dotted lines) (d)–(f) shapes.

cubic superellipsoids, r_1 displays a quasi-logarithmic increase from $r_{1\min} \approx R_1$ to a much larger $r_{1\max} > R_1$. In contrast to cubic superellipsoids, octahedral superellipsoids increase from $r_{1\min} < R_1$ and finally cluster around $r_{1\max} = R_1$. Moreover, for both cubic and octahedral shapes, the r_1 distributions exhibit greater deviations than those of spheroid superellipsoids when $FI = \frac{R_3}{R_2}$ decreases. For the r_2 values of spheroid and octahedral superellipsoids, the cumulative distribution curves display very sharp increasing trends at $r_2 = r_{2\min} \approx R_3 = 1$. When $FI = \frac{R_3}{R_2}$ decreases, the difference between $r_{2\max}$ and R_2 for octahedral superellipsoids increases. In contrast, the r_2 values of cubic superellipsoids display a distribution similar to that of spheroid superellipsoids, where $r_{2\min}$ is always equal to $R_3 = 1$ and $r_{2\max}$ is very close to R_2 . For AR, both the octahedral and spheroid superellipsoids are characterised by $AR_{\max} = EI = \frac{R_2}{R_1} = 1$ and $AR_{\min} = FI = \frac{R_3}{R_2}$, and small deviations between AR_{\min} and FI are observed for cubic superellipsoids when FI decreases.

3.1.3. Case III: Monosized scalene superellipsoids

In Fig. 8, the 2D sizes (r_1 and r_2) and ARs of monosized scalene superellipsoids are statistically illustrated using cumulative distribution curves. As shown in Fig. 8a and d, the variations in r_1 for different ϵ and $EI = \frac{R_2}{R_1}$ values exhibit trends similar to those for prolate superellipsoids, as shown in Fig. 7a and d. Notably, r_1 varies within a broader interval as $EI = \frac{R_2}{R_1}$ decreases, and the curves for both cubic and octahedral superellipsoids exhibit less divergence from the curves for spheroid particles. Likewise, the variations in r_2 for different ϵ and $FI = \frac{R_3}{R_2}$ values are similar to those for oblate superellipsoids, as shown in Fig. 7b and e. However, greater deviations with respect to $r_{2\min}$

($r_{2\max} < R_2$) are observed for the octahedral shape when $FI = \frac{R_3}{R_2}$ increases. Moreover, $r_{2\max}$ for the cubic shape ($r_{2\max} > R_2$) and octahedral shape ($r_{2\max} < R_2$) display large deviations from R_2 as $FI = \frac{R_3}{R_2}$ increases. For AR, as shown in Fig. 8c and f, the AR_{\max} values of all three types of superellipsoids approach 1.0. The AR_{\min} values for the spheroid shape exhibit good agreement with EI and FI ($EI = FI$) for the generated scalene particles). However, the AR_{\min} values of the cubic-shaped superellipsoids are slightly larger than those for spheroid superellipsoids, and the AR_{\min} values of octahedral superellipsoids are smaller than those of spheroid superellipsoids.

3.2. Correlation between 3D geometries and 2D results

Based on the above observations from the statistical distribution of the sizes (r_1 and r_2) and AR values obtained from the 2D projections, some hypotheses can be concluded as follows:

- (1) R_1 of the 3D particles is correlated with $r_{1\max}$ of the 2D projections;
- (2) R_2 of the 3D particles is correlated with $r_{1\min}$ and $r_{2\max}$;
- (3) R_3 of the 3D particles is related to $r_{2\min}$ of the 2D projections; and
- (4) EI and FI are potentially correlated with AR_{\min} and AR_{\max} .

To test the above hypotheses, the $r_{1\max}$, $r_{1\min}$, $r_{2\max}$, $r_{2\min}$, AR_{\max} and AR_{\min} values of the generated superellipsoids are compared with R_1 , R_2 , R_3 , EI and FI using correlation analysis. The scatter diagrams of 3D descriptors plotted against those of the 2D descriptors are shown in Figs. 9–13.

As illustrated in Fig. 9, for spheroid (in red) and octahedral (in

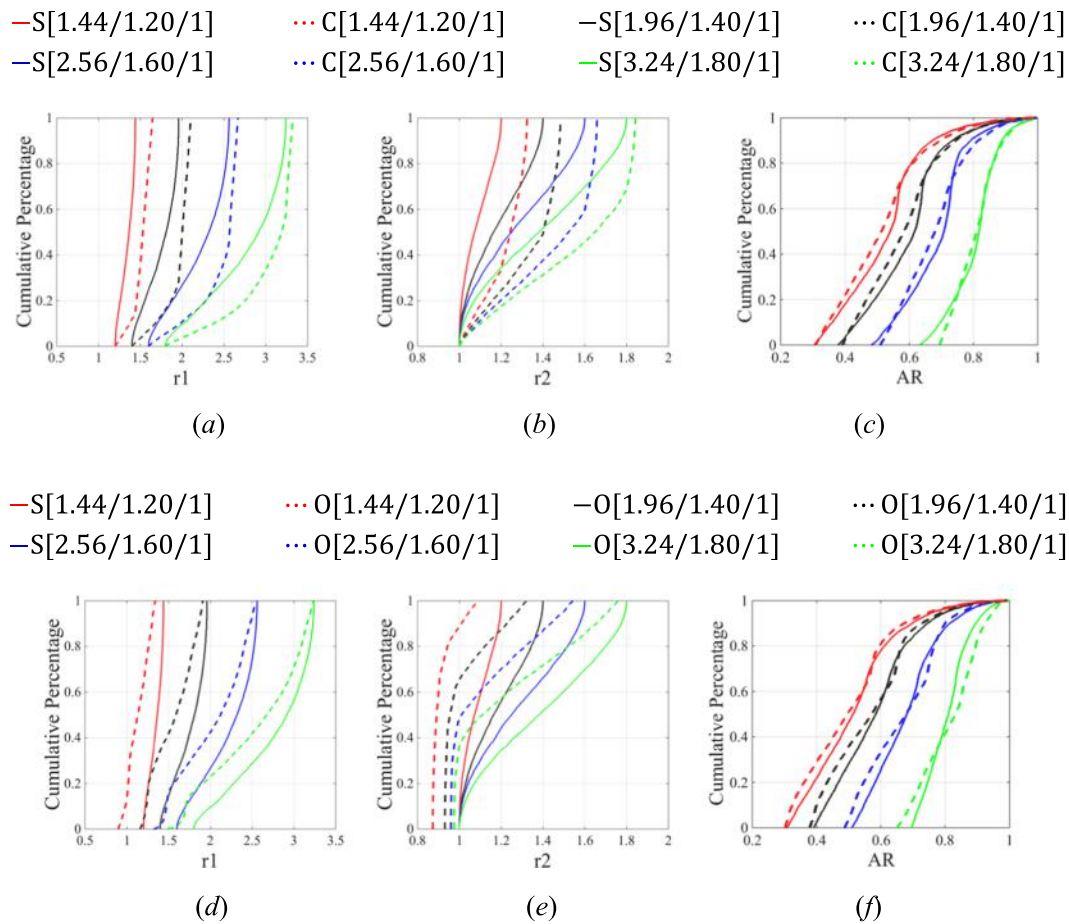


Fig. 8. Comparison of scalene superellipsoids involving spheroids (denoted as S with solid lines) with cubic (denoted as C with dotted lines) (a)–(c) and octahedral (denoted as O with dotted lines) (d)–(f) shapes.

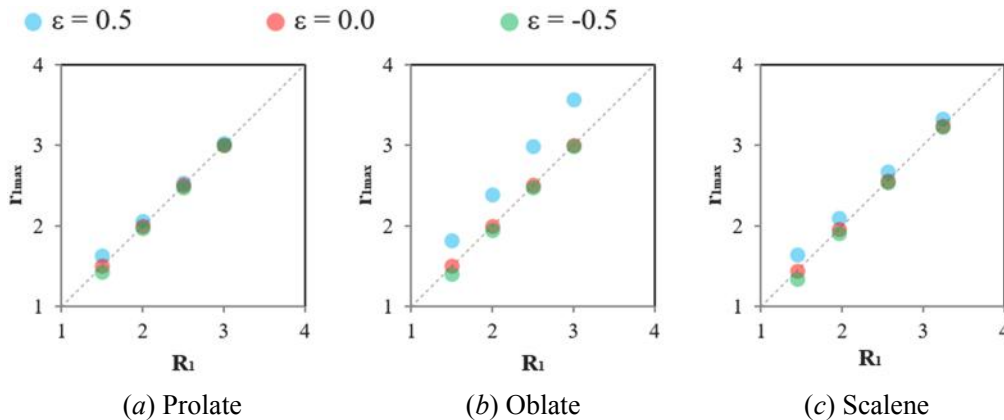


Fig. 9. Comparison of R_1 versus r_{1max} for prolate (a), oblate (b) and scalene (c) superellipsoids.

green) superellipsoids, all r_{1max} values match the corresponding R_1 values. For cubic superellipsoids (in blue), r_{1max} exhibits good agreement with R_1 for the prolate and scalene cases but is slightly larger than R_1 for the oblate case. For R_3 , Fig. 10 shows that r_{2min} is always very close to R_3 for spheroid (in red) and cubic (in blue) superellipsoids but that the values for octahedral superellipsoids (in green) display slight deviations.

As illustrated in Fig. 11, for spheroid superellipsoids, r_{1min} , r_{2max} and their mean value r_{mean} are equal to R_2 in all cases. Cubic superellipsoids exhibit r_{1min} values very close to R_2 , while their r_{2max} and r_{mean} values that are slightly larger than R_2 . In terms of octahedral superellipsoids,

r_{2max} is quite similar to R_2 for the prolate and scalene cases, but the corresponding values are smaller for the oblate case. The r_{1min} and r_{mean} values of octahedral superellipsoids are linearly related to R_2 but consistently smaller.

As shown in Fig. 12, AR_{min} is linearly correlated with EI for all prolate- and scalene-shaped superellipsoids but exhibits no correlation with EI for the oblate case. In contrast, AR_{max} displays no correlation with EI for the prolate and scalene cases but is equal to EI for the oblate case.

As illustrated in Fig. 13, AR_{max} is only equal to FI for prolate-shaped particles, and there is no correlation between AR_{max} and FI for oblate or

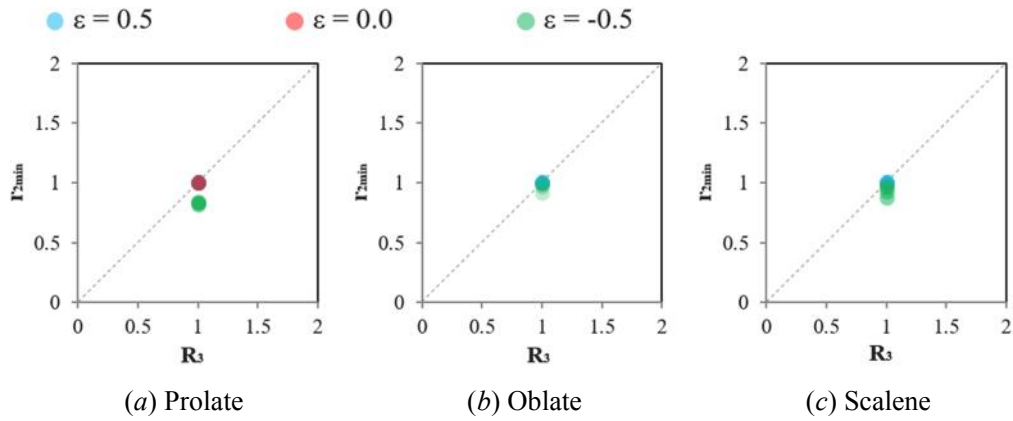


Fig. 10. Comparison of R_3 versus r_{2min} for prolate (a), oblate (b) and scalene (c) superellipsoids.

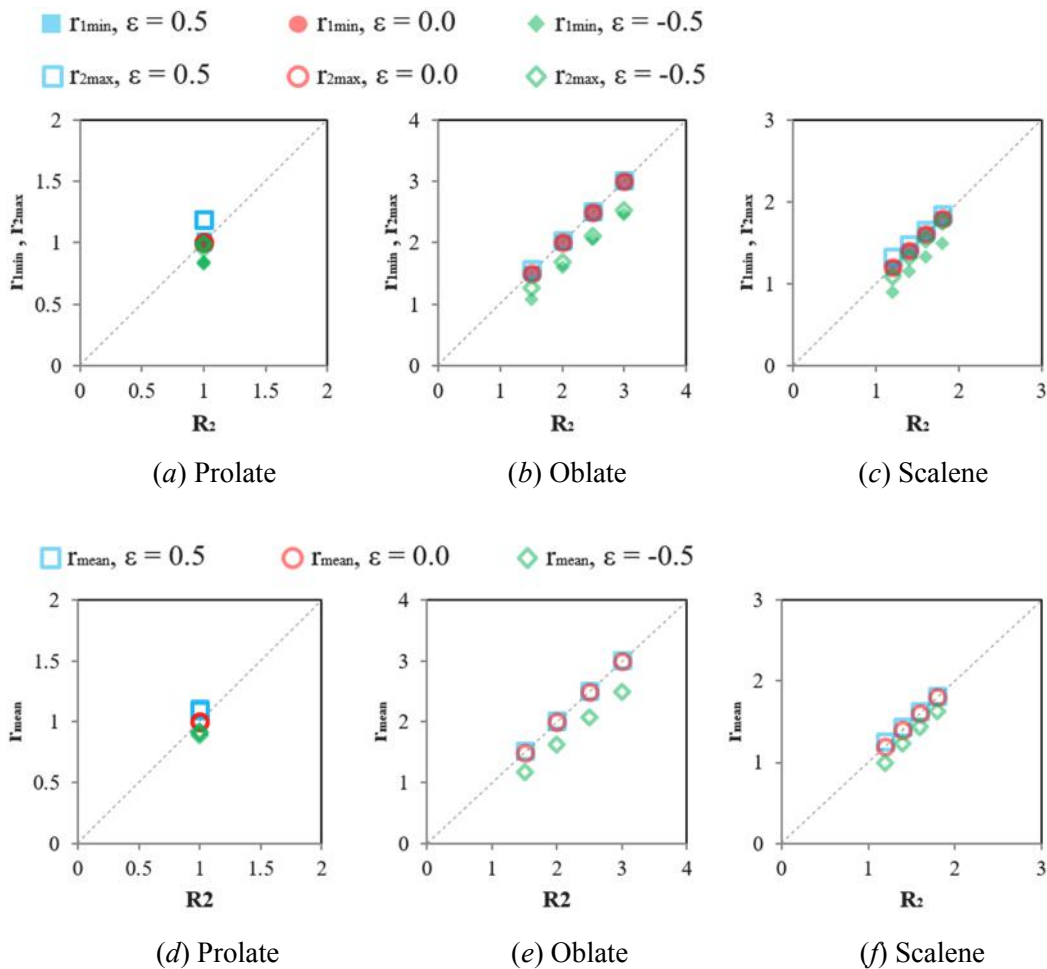


Fig. 11. Comparison of R_2 versus r_{1min} and r_{2max} for prolate (a), oblate (b) and scalene (c) superellipsoids; comparison of R_2 versus $r_{mean} = (r_{1min} + r_{2max})/2$ for prolate (d), oblate (e) and scalene (f) superellipsoids.

scalene particles. In contrast, AR_{min} exhibits a significant correlation with FI for oblate and scalene particles and no correlation with FI for prolate particles. In conclusion, both AR_{min} and AR_{max} have inconsistent relationships with EI and FI for various particle shapes.

3.3. Conclusions from the study of monosized superellipsoids

The correlation analysis provides preliminary insight into the potential of interpreting 3D descriptors with 2D parameters. The following conclusions can be drawn from the results of the proposed

prediction methods:

- (1) r_{1max} of 2D projections can be directly used to predict R_1 for a 3D particle;
- (2) r_{1min} , r_{2max} and their mean value $r_{mean} = (r_{1min} + r_{2max})/2$ can all estimate R_2 with minor error. In this study, r_{mean} is used to infer R_2 directly;
- (3) r_{2min} from particle projections can be employed as an estimator of R_3 ;
- (4) AR_{max} and AR_{min} cannot be used to predict EI or FI because the

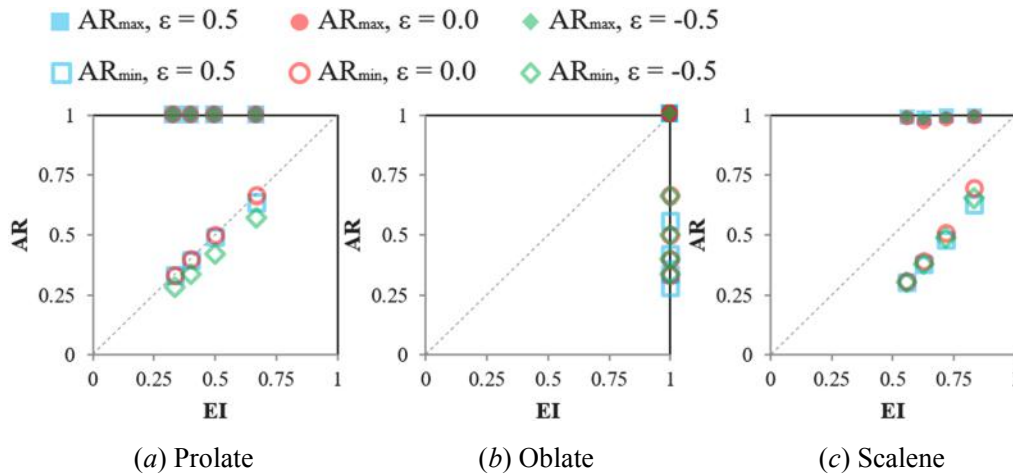


Fig. 12. Comparison of AR_{max} and AR_{min} versus EI for prolate (a), oblate (b) and scalene (c) superellipsoids.

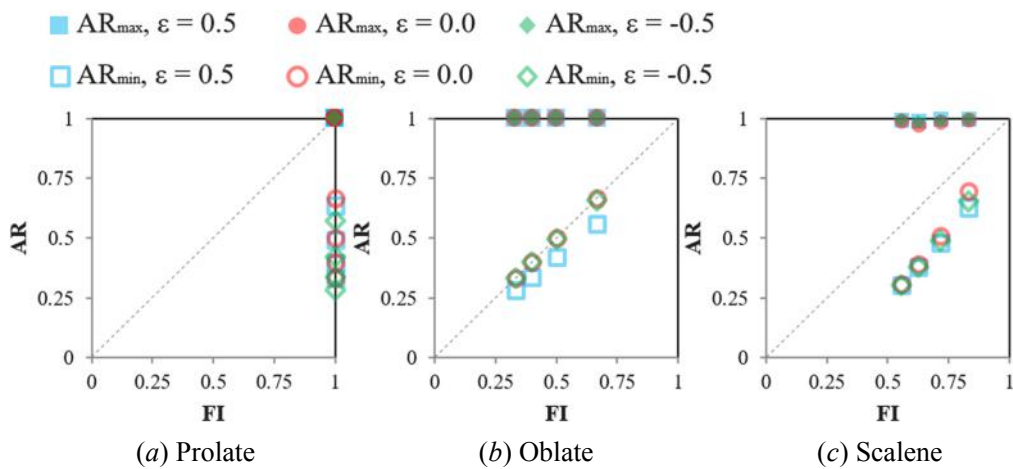


Fig. 13. Comparison of AR_{max} and AR_{min} versus FI for prolate (a), oblate (b) and scalene (c) superellipsoids.

relationships between them are unpredictable if the shape (prolate, oblate or scalene) of a particular particle is unknown; and

- (5) Because R_1 , R_2 , and R_3 can be well estimated by r_{1max} , r_{mean} and r_{2min} , two alternative 2D shape parameters, namely, $EI2D = r_{mean}/r_{1max}$ and $FI2D = r_{2min}/r_{mean}$, are proposed to interpret EI and FI for 3D particles.

4. Study of randomised superellipsoids with various geometries

In practice, the dimensions (R_1 , R_2 , R_3) and shapes (ϵ) of target particles are always unknown, and these values can be randomly distributed within certain ranges. Moreover, when scanning real particles with a dynamic imaging system, only a certain number of projection images can be obtained for a single particle. Additionally, various errors may influence the results if the projection number is small or if the shapes of superellipsoids vary over a broad range. We can obtain further insight into the influences of these factors through studies of randomised superellipsoids with various geometries. Three groups of superellipsoids are generated with various R_1 , R_2 , R_3 and ϵ values using the uniform random operator. For each group, R_1 , R_2 and R_3 are uniform random variables ranging from 1.0 to 4.0. The values of ϵ are randomly taken from three ranges: $\epsilon = 0$, $\epsilon \in (-0.5, 0.5)$, and $\epsilon \in (-1, 1)$. Each group consists of 500 particles. Fig. 14 shows 100 example particles in a Zingg diagram. Notably, the generated superellipsoids become equant in shape when EI and FI approach 1.0 and exhibit disc-like, rod-like and blade-like shapes when EI and FI decrease.

4.1. Influence of variations in shape asphericity on the prediction performance

The degree to which the shape of a superellipsoid deviates from a spheroid is reflected by the adopted index of shape asphericity ϵ . The more the ϵ value deviates from 0, the more aspherical a particle shape. In this section, the variations in shape asphericity are constrained by the absolute maximum value $|\epsilon|_{max}$. To study the influence of variations in shape asphericity on prediction performance, particles are generated with $|\epsilon|_{max} = 0$ ($\epsilon_i = 0$), $|\epsilon|_{max} = 0.5$ ($\epsilon_i \in (-0.5, 0.5)$), and $|\epsilon|_{max} = 1$ ($\epsilon_i \in (-1, 1)$), as shown in Fig. 14. To simulate a limited number of projections, all particles are equally projected 5 times each. Then, 2D descriptors, including r_{1max} , r_{mean} , r_{2min} , EI2D and FI2D, are measured from projected images and plotted against the 3D parameters R_1 , R_2 , R_3 , EI, and FI of the same particle.

Fig. 15a–c illustrates the scatter diagrams when r_{1max} , r_{mean} and r_{2min} are used to predict the values of R_1 , R_2 and R_3 , respectively. Clearly, linear correlations between R_1 , R_2 and R_3 and r_{1max} , r_{mean} and r_{2min} can still be observed (similar to the results of monosized superellipsoids shown in Section 3.2). Although the degree of scatter generally increases between individual $r_{2D} \rightarrow R_{3D}$ pairs when $|\epsilon|_{max}$ increases from 0.0 to 1.0, the data points are essentially clustered around the equivalent line of $r_{2D} = R_{3D}$ in all three cases. The R_1 points above the diagonal are more concentrated than those below the diagonal. For both R_2 and R_3 , more points are plotted above the diagonal for $|\epsilon|_{max} = 0$, and the degree of scatter drastically varies as $|\epsilon|_{max}$ changes. The statistics associated with R_2 and R_3 contribute more to the scatter

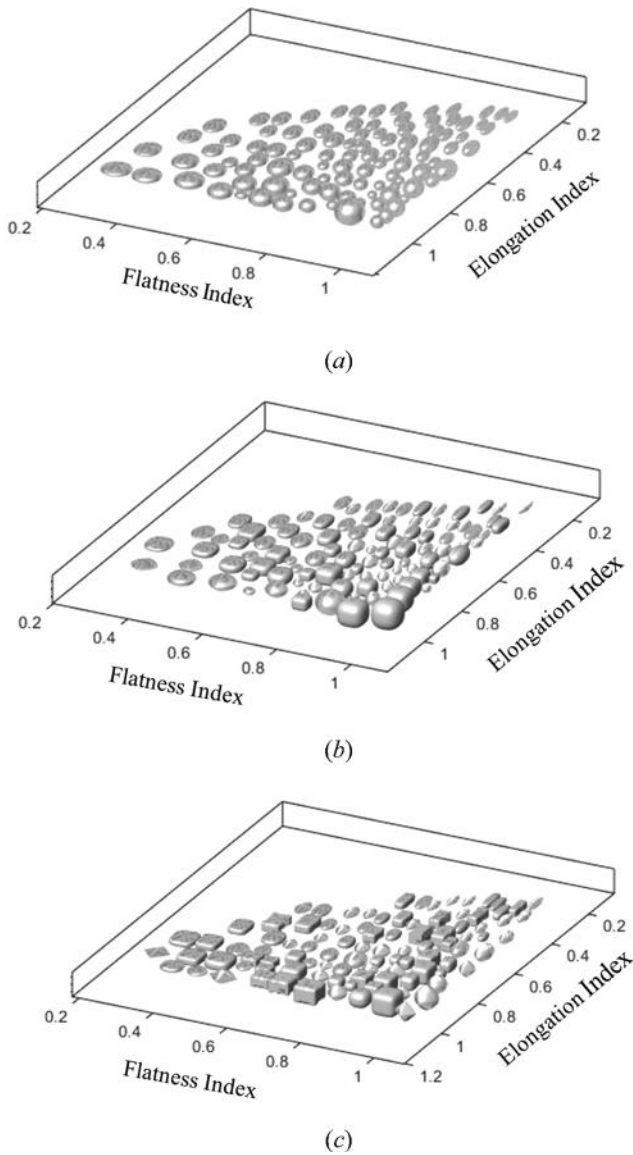


Fig. 14. Examples of randomised 3D superellipsoids in a Zingg diagram (a) $|\epsilon|_{\max} = 0$; (b) $|\epsilon|_{\max} = 0.5$; (c) $|\epsilon|_{\max} = 1.0$

than those of R_1 . For shapes, the degree of scatter of EI above the diagonal increases with increasing $|\epsilon|_{\max}$, and FI exhibits more scatter below the diagonal when $|\epsilon|_{\max}$ increases.

4.2. Influence of projection number on the prediction performance

To determine the effect that the projection number has on the prediction of 3D descriptors, superellipsoids with $|\epsilon|_{\max} = 0.5$ are generated, and 2D descriptors are measured for various numbers of projections ($n = 2$, $n = 5$ and $n = 20$).

Fig. 16a–c shows the scatter diagrams used to estimate R_1 , R_2 and R_3 for projection numbers of 2, 5 and 20. The predictions of all 3D size parameters display fewer deviations as the projection number increases. The values of particles with 2 projections exhibit notable fluctuations, and those of particles with 5 and 20 projections diverge less. The results for shape factors EI and FI are plotted in Fig. 16d–f. Both the correlation and concentration of points with respect to the diagonal decrease with decreasing projection number.

In conclusion, a decrease in the projection number has an adverse impact on the precision of predicting 3D parameters from 2D descriptors. For superellipsoids with $|\epsilon|_{\max} = 0.5$, 5 and 20 projections lead

to relatively high precision (more projection time yields a more accurate result), and 2 projections result in much lower accuracy.

4.3. Strategy for predicting the sizes and shapes of particles with unknown geometries

The average relative errors \bar{E}_{Size} and \bar{E}_{Shape} are used to quantify the prediction accuracy of particle sizes (R_1 , R_2 , R_3) and particle shapes (EI, FI). The \bar{E}_{Size} and \bar{E}_{Shape} values for m numbers of randomly generated superellipsoids are computed as follows.

$$\bar{E}_{\text{Size}} = \frac{\sum \left[\left(\frac{|R_1 - r_{1\max}|}{R_1} + \frac{|R_2 - r_{2\text{mean}}|}{R_2} + \frac{|R_3 - r_{2\min}|}{R_3} \right) / 3 \right]}{m} \quad (17)$$

$$\bar{E}_{\text{Shape}} = \frac{\sum \left[\left(\frac{|\text{EI} - \text{EI2D}|}{\text{EI}} + \frac{|\text{FI} - \text{FI2D}|}{\text{FI}} \right) / 2 \right]}{m} \quad (18)$$

Superellipsoids with R_1, R_2 and $R_3 \in [1, 4]$ are randomly generated and projected with various combinations of $|\epsilon|_{\max}$ and projection numbers. For each combination, the average relative errors, \bar{E}_{Size} and \bar{E}_{Shape} , are subsequently computed. To guarantee the stability of the resulting \bar{E}_{Size} and \bar{E}_{Shape} values, for each $|\epsilon|_{\max}$ and projection number pair, 5000 superellipsoids are generated. The results of \bar{E}_{Size} and \bar{E}_{Shape} versus $|\epsilon|_{\max}$ and the projection number are plotted in Fig. 17 and Fig. 18, respectively. The minimum projection number = 2 and the largest value of $|\epsilon|_{\max} = 1.0$ results in peaks in the \bar{E}_{Size} and \bar{E}_{Shape} plots, indicating low accuracy in predicting the 3D size and shape factors from 2D projections. The maxima of \bar{E}_{Size} and \bar{E}_{Shape} are 0.170 and 0.175, respectively. As the projection number increases and the divergence of shape asphericity decreases, \bar{E}_{Size} and \bar{E}_{Shape} both rapidly decrease. The valleys of both \bar{E}_{Size} and \bar{E}_{Shape} in the plot corresponding to the most accurate prediction occur at a projection number of 20 and $|\epsilon|_{\max} = 0$. The minima of \bar{E}_{Size} and \bar{E}_{Shape} are 0.01 and 0.02, respectively.

Based on these results, a preliminary prediction strategy for aspherical particles with unknown geometries is suggested as follows.

- (1) Determine the shape variation $|\epsilon|_{\max}$ and the allowable values of the prediction error \bar{E}_{Size} and \bar{E}_{Shape} according to the target application or case.
- (2) Based on the estimated $|\epsilon|_{\max}$ and the desired \bar{E}_{Size} and \bar{E}_{Shape} values, find the corresponding projection numbers m_{Size} and m_{Shape} based on the results shown in Fig. 17 and Fig. 18.
- (3) If only the size or shape is of interest, use the corresponding projection numbers m_{Size} or m_{Shape} for particle projection and 3D geometry prediction. If both the size and shape are of interest, use the maximum value among m_{Size} and m_{Shape} .

5. Applications and future work

5.1. Application to 3D laser-scanned cobble particles

Real cobble particles scanned by 3D laser scanning were used to assess the performance of the proposed approach for aspherical real particles. The cobble is named Xiangjiang River cobble (XRC), and it is a typical aggregate material in South China. Nie et al. [42] evaluated the 3D shapes of cobblestones scanned at a 3D laser scanner facility located at Central South University, China. In total, 50 cobbles with sphere-, blade-, disc- and rod-like shapes were selected according to the classification system suggested by Zingg (see Fig. 19). As shown in Fig. 20, the cobbles had a minimum mean curvature-based roundness value of 0.3. Based on [42], the mean curvature-based roundness changes as ϵ varies (shown as a blue dashed line in Fig. 20). It can be inferred from the figure that the most aspherical cobble (with a mean curvature-based roundness of 0.3) roughly corresponds to a superellipsoid with $\epsilon = 0.7$.

To examine the performance of the proposed approach, the

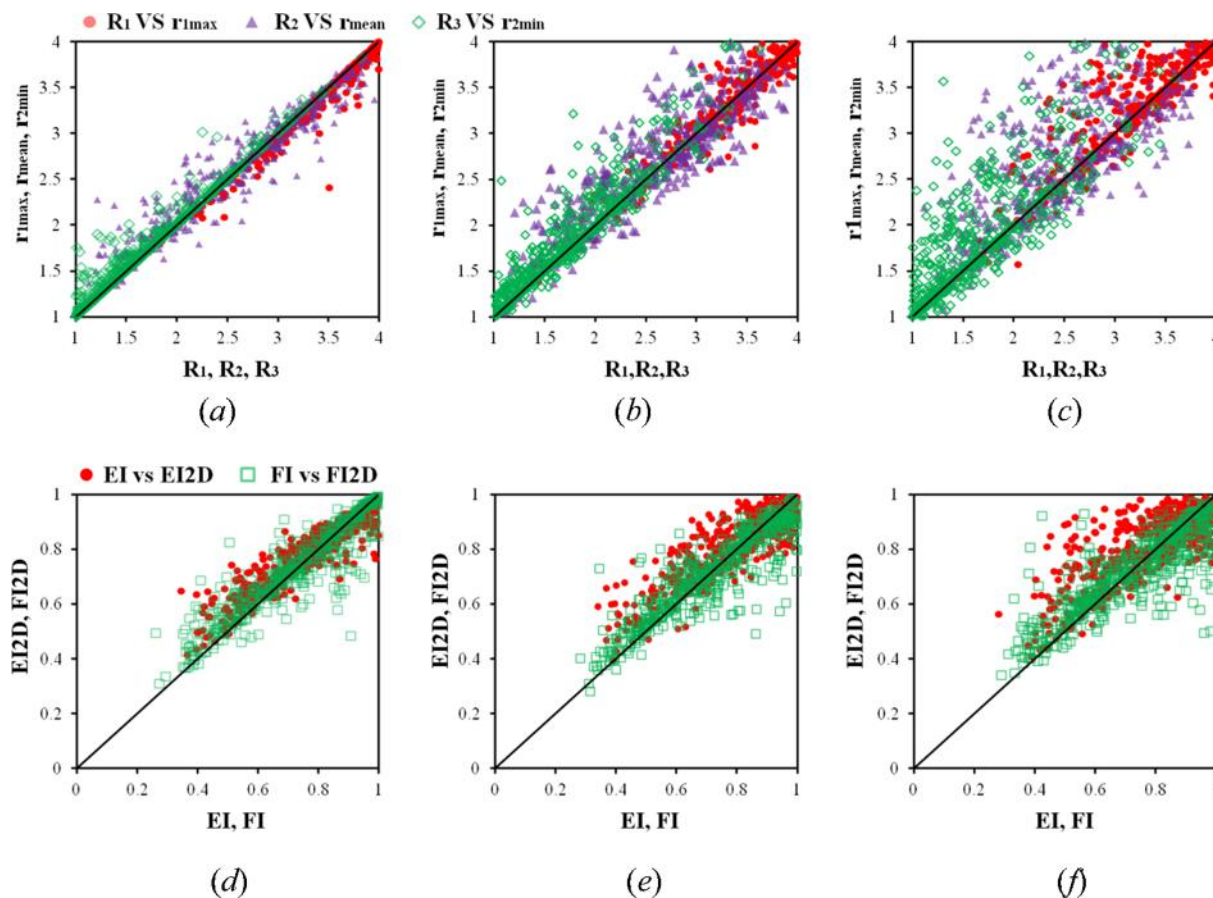


Fig. 15. R_1 , R_2 , and R_3 predicted by r_{1max} , r_{mean} , and r_{2min} with (a) $|\epsilon|_{max} = 0$, (b) $|\epsilon|_{max} = 0.5$, and (c) $|\epsilon|_{max} = 1.0$; EI and FI predicted by EI2D and FI2D with (d) $|\epsilon|_{max} = 0$, (e) $|\epsilon|_{max} = 0.5$, and (f) $|\epsilon|_{max} = 1.0$

projection number of each particle is first determined based on the prediction strategy proposed in Section 4.3. Given that the acceptable prediction error is 0.1 and $|\epsilon|_{max}$ is 0.7, the optimal projection number was determined to be 10. Subsequently, each cobble particle was randomly projected 10 times to acquire 2D images. With the obtained 2D projections of the cobbles, the proposed prediction method was employed to estimate the 3D sizes and shapes. The statistical results of the predicted sizes and shapes are compared with the actual values in Fig. 21. The cumulative distribution curves of the sizes exhibit good agreement, and the shape results are promising. Overall, based on the suggested prediction strategy, the sizes (R_1 , R_2 , R_3) and shapes (EI, FI) of the real cobbles were reasonably predicted based on a limited number of 2D random projections.

5.2. Discussion of future developments

The proposed work still has several limitations. Thus, the following work will be performed in the future to promote the prediction of the 3D geometry of large granular particles with 2D random projections.

(1) Predicting the geometry of real aggregates during particle falling and rolling

Instead of acquiring the virtual digital projections from the 3D laser-scanned particle model, the real 2D random projected images can be obtained through the falling and rolling of the 3D particle along an inclined slope with high-speed shooting. The conceptual plan for the dynamic scanning of large aggregates is illustrated in Fig. 22. As long as the random projected images are acquired, the proposed method can be used to predict the principal dimensions, elongations and flatness of the

particles.

(2) Assessing complex shape effects on prediction accuracy

The adopted superellipsoids cannot fully represent realistic granular particles with high complexity and irregular shape; e.g., the effects of asymmetry are not considered. The extensive shape variations of realistic granular particles will decrease the prediction accuracy and require high projection numbers during scanning. The studied particle shapes include only elongation and flatness properties, which are associated with the particle form. The angularity and roughness properties are not considered. Possible solutions to address these drawbacks are suggested as follows:

I. Effect of particle asymmetry

The proposed superellipsoid model is good at evaluating the particle asphericity effect. However, there is very little research on particle asymmetry. Future work will be performed to employ special models, e.g., the egg-shaped particle (ESP) model [43] and the poly-ellipsoidal grain (PEG) model [44], to quantitatively investigate the effect of the asymmetric shape on the relationship between 3D and 2D geometries.

II. Effect of particle angularity and roughness

Considering that the abovementioned particle models, e.g., superellipsoid, egg-shaped particle, poly-ellipsoidal grain, can hardly reproduce very complex particle shapes, e.g., angularity and roughness, spherical harmonic (SH) analysis [45] will be employed to randomly reconstruct virtual particles with quantitatively controlled angularity

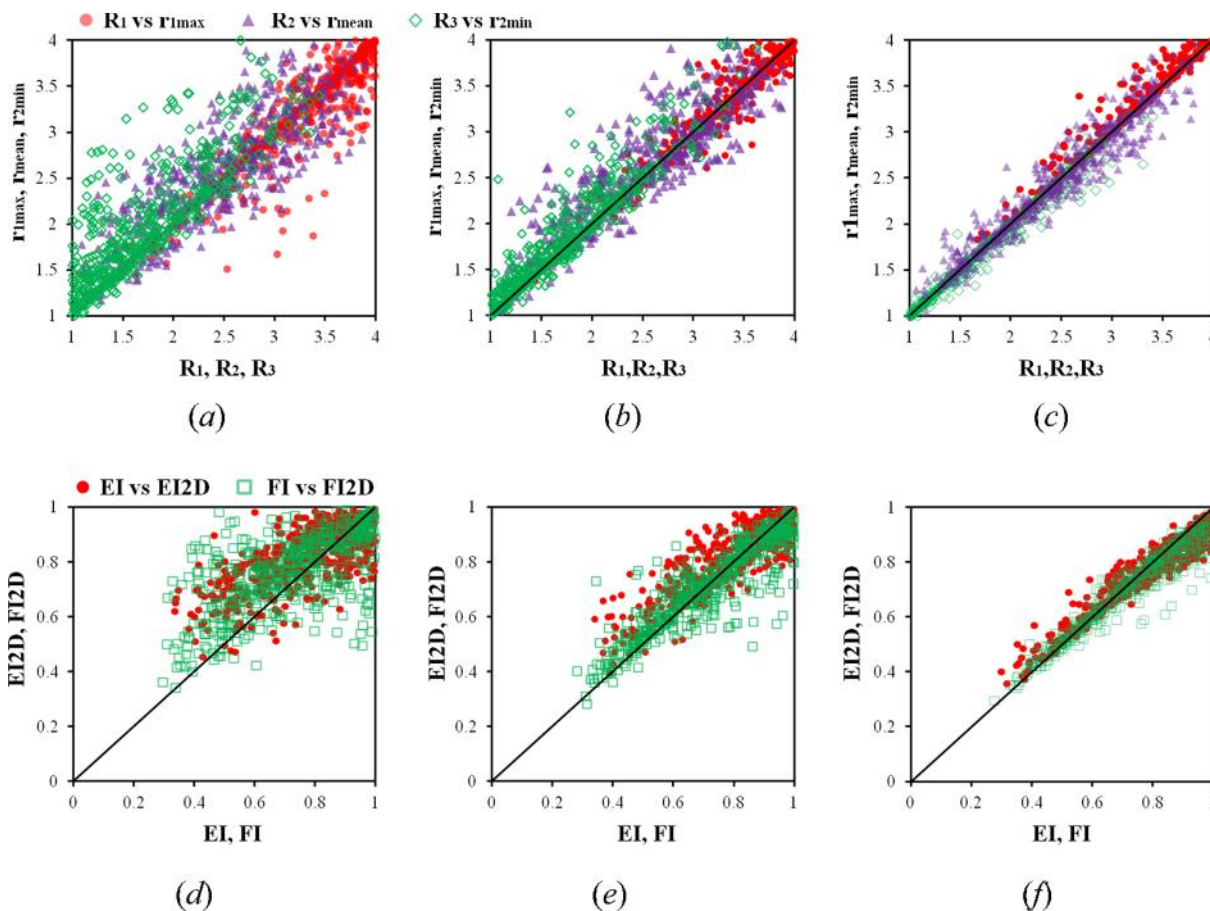


Fig. 16. R_1 , R_2 and R_3 predicted by r_{1max} , r_{mean} and r_{2min} with (a) $n = 2$, (b) $n = 5$, and (c) $n = 10$; EI and FI predicted by EI2D and FI2D with (d) $n = 2$, (e) $n = 5$, and (f) $n = 20$.

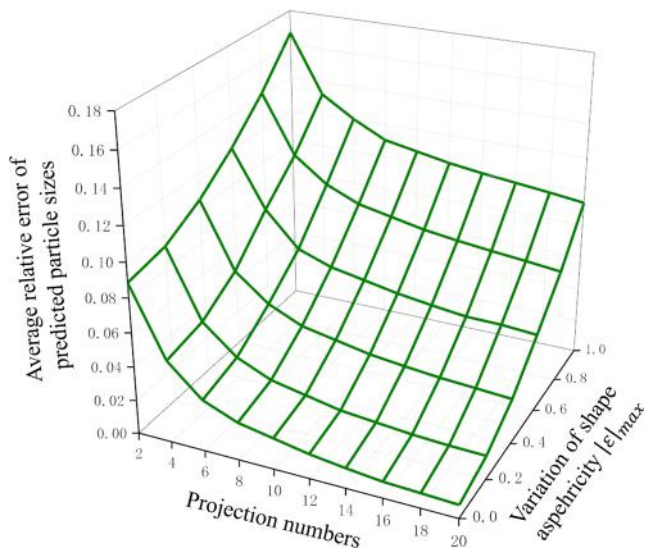


Fig. 17. Contour plot of the average relative error of the predicted particle size \bar{E}_{Size} versus the projection number and variations in shape asphericity.

and roughness features. By evaluating the 2D angularity and roughness of the projections of SH-based particles, it will be possible to quantitatively investigate the ability of predicting more complex 3D particle shapes with 2D random projections.

(3) Reconstructing 3D particles with 2D random projections

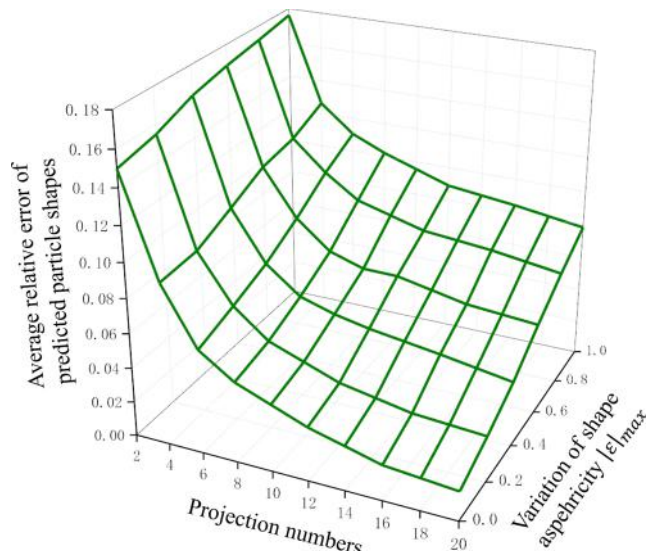


Fig. 18. Contour plot of the average relative error of the predicted particle shape \bar{E}_{Shape} versus the projection number and variations in shape asphericity.

Reverse construction of a 3D digital model of real particles has attracted research interest, motivated by the objective to generate realistic shapes for the discrete element modelling of granular particles. Since the 3D sizes of the real particle can be well predicted based on the proposed approach, future work will be conducted to reconstruct the 3D particle from its 2D random projections. Possible solutions will

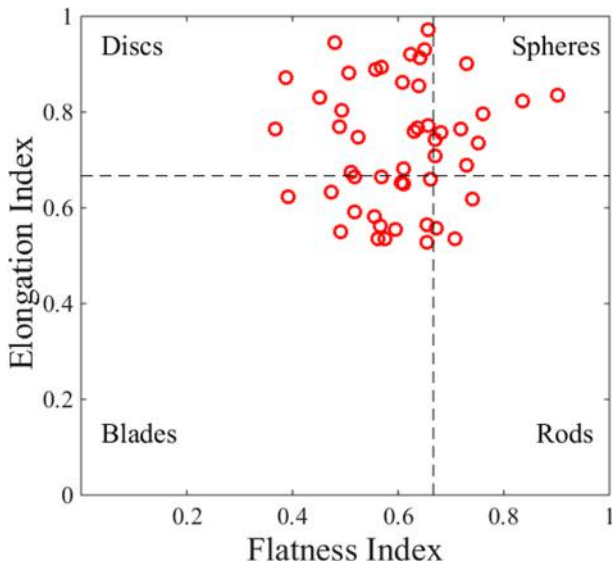


Fig. 19. Zingg diagram summarising the EI and FI values of the 50 cobbles obtained.

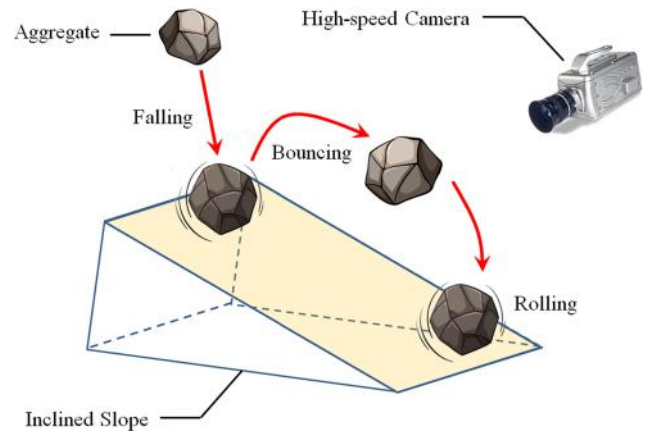


Fig. 22. Illustration of conceptual plan for dynamic scanning of large aggregates.

involve using the appropriate 2D projected images to form a 3D solid skeleton, followed by using surface interpolation to generate the 3D particle. By combining this approach with the dynamic scanning device being designed (shown in Fig. 22), a cost-efficient 3D particle reconstruction system will be developed as an alternative scheme to the existing high-cost systems, e.g., X-ray CT and 3D laser scanner.

6. Conclusions

Superellipsoids and their projected images were used to examine the relationships among 3D and 2D particle size and shape characteristics. A prediction strategy for aspherical particles with unknown geometries was suggested based on a statistical analysis of the results. A verification of the methodology was performed based on an application involving real cobble particles. The following major observations were made in this study.

- (1) The cumulative distribution curves of 2D sizes and shapes exhibit specific trends for different types of monosized superellipsoids.
- (2) The r_{1max} , r_{mean} and r_{2min} values of the 2D projections can be used to predict R_1 , R_2 and R_3 for a 3D particle.
- (3) The EI and FI values of the 3D particles are difficult to infer with AR values but can be predicted by EI2D (r_{mean}/r_{1max}) and FI2D

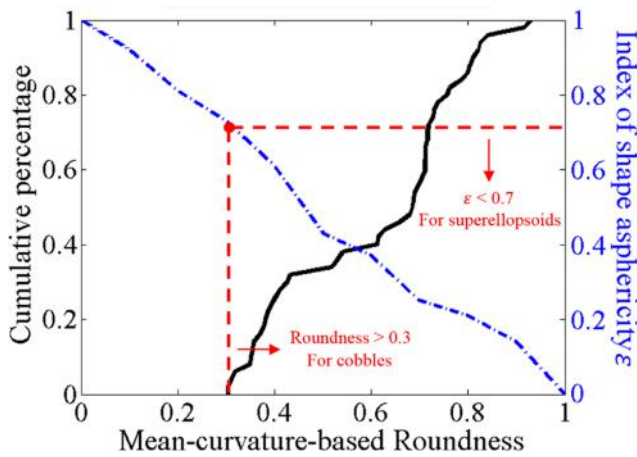
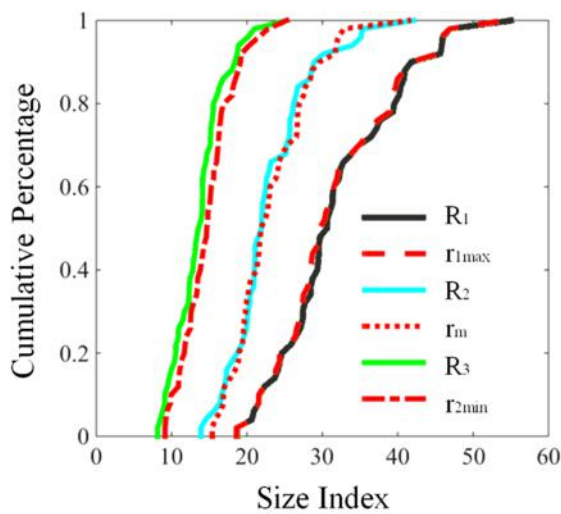
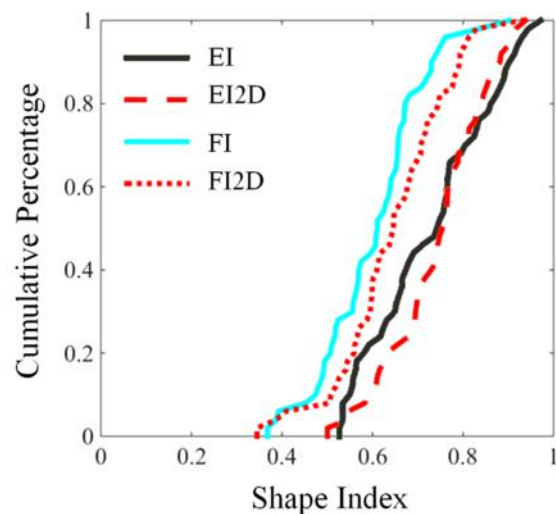


Fig. 20. Mean curvature-based roundness of cobbles and the corresponding ϵ -value range of superellipsoids.



(a)



(b)

Fig. 21. Statistical distributions of the real (measured from 3D) and predicted (measured from 2D) sizes (a) and shapes (b).

(r_{2min}/r_{1mean}), respectively.

- (4) The particle asphericity and projection number significantly influence the prediction accuracy and should be considered when developing dynamic imaging and scanning methods for industrial applications.
- (5) The proposed prediction strategy displayed promising prediction capability, as demonstrated by comparing the cumulative distributions of the sizes and shapes of 3D laser-scanned real cobble particles with the values inferred from their 2D projections.

In summary, based on easy-to-visualise superellipsoids, this study

Appendix A. Abbreviations

LPSA	Laser particle size analyser
SGA	Segmentation-based Gradation Analyser
ERPC	Electrical resistance particle counter
PDIP	Particle digital image processor
EI	Elongation index
FI	Flatness index
AR	Aspect ratio
EI2D	Predicted elongation index from 2D projections
FI2D	Predicted flatness index from 2D projections

Appendix B. Symbols

R_1	Longest semi-axis length for a 3D particle
R_2	Intermediate semi-axis length for a 3D particle
R_3	Shortest semi-axis length for a 3D particle
ε	Index of shape asphericity
r_1	Longest semi-axis length for a 2D projected particle
r_{1max}	Maximum value of r_1 among random 2D projections
r_{1min}	Minimum value of r_1 among random 2D projections
r_2	Shortest semi-axis length for a 2D projected particle
r_{2max}	Maximum value of r_2 among random 2D projections
r_{2min}	Minimum value of r_2 among random 2D projections
r_{mean}	Average value between r_{1min} and r_{2max}

References

- [1] Masch FD, Denny KJ. Grain size distribution and its effect on the permeability of unconsolidated sands. *Water Resour Res* 1966;2:665–77.
- [2] Zhang B-Y, Jie Y-X, Kong D-Z. Particle size distribution and relative breakage for a cement ellipsoid aggregate. *Comput Geotech* 2013;53:31–9.
- [3] Sohn HY, Moreland C. The effect of particle size distribution on packing density. *Can J Chem Eng* 1968;46:162–7.
- [4] Zhao S, Zhou X. Effects of particle asphericity on the macro- and micro-mechanical behaviors of granular assemblies. *Granular Matter* 2017;19:38.
- [5] Santamarina J, Cho G-C. Soil behaviour: The role of particle shape. *Advances in geotechnical engineering: The skempton conference*. Citeseer 2004:604–17.
- [6] Lu M, McDowell G. The importance of modelling ballast particle shape in the discrete element method. *Granular Matter* 2007;9:69.
- [7] Zhao S, Zhang N, Zhou X, Zhang L. Particle shape effects on fabric of granular random packing. *Powder Technol* 2017;310:175–86.
- [8] Wouterse A, Williams SR, Philipse AP. Effect of particle shape on the density and microstructure of random packings. *J Phys: Condens Matter* 2007;19:406215.
- [9] Kyrilyuk AV, Philipse AP. Effect of particle shape on the random packing density of amorphous solids. *physica status solidi (a)* 2011;208:2299–302.
- [10] Gong J, Nie Z, Zhu Y, Liang Z, Wang X. Exploring the effects of particle shape and content of fines on the shear behavior of sand-fines mixtures via the DEM. *Comput Geotech* 2019;106:161–76.
- [11] Zhao S, Evans TM, Zhou X. Shear-induced anisotropy of granular materials with rolling resistance and particle shape effects. *Int J Solids Struct* 2018;150:268–81.
- [12] Cleary PW. The effect of particle shape on simple shear flows. *Powder Technol* 2008;179:144–63.
- [13] Payan M, Khoshghalb A, Senetakis K, Khalili N. Effect of particle shape and validity of Gmax models for sand: A critical review and a new expression. *Comput Geotech* 2016;72:28–41.
- [14] Cho G-C, Dodds J, Santamarina JC. Particle shape effects on packing density, stiffness, and strength: natural and crushed sands. *J Geotech Geoenviron Eng* 2006;132.
- [15] Nie Z, Liang Z, Wang X. A three-dimensional particle roundness evaluation method. *Granular Matter* 2018;20:32.
- [16] Zhihong N, Zhengyu L, Xiang W, Jian G. Evaluation of granular particle roundness using digital image processing and computational geometry. *Constr Build Mater* 2018;172:319–29.
- [17] Su D, Yan W. Quantification of angularity of general-shape particles by using Fourier series and a gradient-based approach. *Constr Build Mater* 2018;161:547–54.
- [18] Su D, Yan W. 3D characterization of general-shape sand particles using microfocus X-ray computed tomography and spherical harmonic functions, and particle regeneration using multivariate random vector. *Powder Technol* 2018;323:8–23.
- [19] O'Sullivan C, Cavarretta I, Fonseca J, Altuhaifi F. Quant Eval Particle Morphol 2013.
- [20] Wang X, Liang Z, Nie Z, Gong J. Stochastic numerical model of stone-based materials with realistic stone-inclusion features. *Constr Build Mater* 2018.
- [21] Mollon G, Zhao J. 3D generation of realistic granular samples based on random fields theory and Fourier shape descriptors. *Comput Methods Appl Mech Eng* 2014;279:46–65.
- [22] Mollon G. Fourier–Voronoi-based generation of realistic samples for discrete modelling of granular materials. *Granular Matter* 2012;14:621–38.
- [23] Witt W, Köhler U, List J. Current limits of particle size and shape analysis with high speed image analysis. Citeseer 2006.
- [24] List J, Köhler U, Witt W. Dynamic image analysis extended to fine and coarse particles. *Part. Syst. Anal. Edinburgh* 2011;1.
- [25] Abeynaike A, Sederman A, Khan Y, Johns M, Davidson J, Mackley M. The experimental measurement and modelling of sedimentation and creaming for glycerol/biodiesel droplet dispersions. *Chem Eng Sci* 2012;79:125–37.
- [26] Monazam ER, Spenik J, Shadle LJ. Fluid bed adsorption of carbon dioxide on immobilized polyethylenimine (PEI): kinetic analysis and breakthrough behavior. *Chem Eng J* 2013;223:795–805.
- [27] Cavarretta I, O'Sullivan C, Ibraim E, Lings M, Hamlin S, Wood DM. Characterization of artificial spherical particles for DEM validation studies. *Particuology* 2012;10:209–20.
- [28] Altuhaifi F, Coop M. Micro-morphological changes in granular soils, *International Symposium on Geomechanics and Geotechnics: From Micro to Macro, IS-Shanghai 2010*, 2011.
- [29] Yu W, Muteki K, Zhang L, Kim G. Prediction of bulk powder flow performance using comprehensive particle size and particle shape distributions. *J Pharm Sci* 2011;100:284–93.
- [30] Sandler N, Wilson D. Prediction of granule packing and flow behavior based on

- particle size and shape analysis. *J Pharm Sci* 2010;99:958–68.
- [31] cavarretta I, coop M, O'sullivan C. The influence of particle characteristics on the behaviour of coarse grained soils. *Géotechnique* 2010;60(6):413–23. <https://doi.org/10.1680/geot.2010.60.6.413>.
- [32] Kuo C-Y, Frost J, Lai J, Wang L. Three-dimensional image analysis of aggregate particles from orthogonal projections. *Transport Res Record: J Transport Res Board* 1996;98–103.
- [33] Yamamoto K-I, Inoue T, Miyajima T, Doyama T, Sugimoto M. Measurement and evaluation of three-dimensional particle shape under constant particle orientation with a tri-axial viewer. *Adv Powder Technol* 2002;13:181–200.
- [34] Kutay ME, Ozturk HI, Abbas AR, Hu C. Comparison of 2D and 3D image-based aggregate morphological indices. *Int J Pavement Eng* 2011;12:421–31.
- [35] Fonseca J, O'Sullivan C, Coop MR, Lee PD. Non-invasive characterization of particle morphology of natural sands. *Soils Found* 2012;52:712–22.
- [36] Yan W, Su D. Inferring 3D particle size and shape characteristics from projected 2D images: Lessons learned from ellipsoids. *Comput Geotech* 2018;104:281–7.
- [37] Yan WM, Su D. Evaluation of three-dimensional particle shape index from projected two-dimensional image. *Géotechnique Lett* 2018;8:336–43.
- [38] Ueda T, Oki T, Koyanaka S. 2D–3D conversion method for assessment of multiple characteristics of particle shape and size. *Powder Technol* 2019;343:287–95.
- [39] Williams JR, Pentland AP. Superquadrics and modal dynamics for discrete elements in interactive design. *Eng Comput* 1992;9:115–27.
- [40] Delaney GW, Cleary PW. The packing properties of superellipsoids. *EPL* 2010;89:275–88.
- [41] Barrett P. The shape of rock particles, a critical review. *Sedimentology* 1980;27:291–303.
- [42] Zhihong N, Xiang W, Zhengyu L, Jian G. Quantitative analysis of the three-dimensional roundness of granular particles. *Powder Technol* 2018.
- [43] Zhou W, Huang Y, Ng TT, Ma G. A geometric potential-based contact detection algorithm for egg-shaped particles in discrete element modeling. *Powder Technol* 2017;327.
- [44] Zhang B, Regueiro R, Druckrey A, Alshibli K. Construction of poly-ellipsoidal grain shapes from SMT imaging on sand, and the development of a new DEM contact detection algorithm. *Eng Comput* 2018;35.
- [45] Su D, Yan WM. 3D characterization of general-shape sand particles using micro-focus X-ray computed tomography and spherical harmonic functions, and particle regeneration using multivariate random vector. *Powder Technol* 2017.